

Quantum Design for Advanced Qubits

Feng-Ming Liu^{1,2,3}, Ming-Cheng Chen^{1,2,3}, Can Wang^{1,2,3}, Shao-Wei Li^{1,2,3}, Zhong-Xia Shang^{1,2,3}, Chong Ying^{1,2,3}, Jian-Wen Wang^{1,2,3}, Cheng-Zhi Peng^{1,2,3}, Xiaobo Zhu^{1,2,3},
Chao-Yang Lu^{1,2,3}, Jian-Wei Pan^{1,2,3}

¹Hefei National Laboratory for Physical Sciences at Microscale and Department of Modern Physics, University of Science and Technology of China, Hefei, Anhui 230026, China

²Shanghai Branch, CAS Centre for Excellence and Synergetic Innovation Centre in Quantum Information and Quantum Physics, University of Science and Technology of China, Shanghai 201315, China ³Shanghai Research Center for Quantum Sciences, Shanghai 201315, China

One sentence summary:

We demonstrate quantum computer-aided design of a new high-performance superconducting quantum processor.

Abstract

Simulations of high-complexity quantum systems, which are intractable for classical computers, can be efficiently done with quantum computers. Similarly, the increasingly complex quantum electronic circuits themselves will also need efficient simulations on quantum computers, which in turn will be important in quantum-aided design for next-generation quantum processors. Here, we implement variational quantum eigensolvers to simulate a Josephson-junction-array quantum circuit, which leads to the discovery of a new type of high-performance qubit, plasonium. We fabricate this new qubit and demonstrate that it exhibits not only long coherence time and high gate fidelity, but also a shrinking physical size and larger anharmonicity than the transmon, which can offer a number of advantages for scaling up multi-qubit devices. Our work opens the way to designing advanced quantum processors using existing quantum computing resources.

Main text

The past half century has witnessed the rapid development of integrated circuits from several to billions of electronic components. A key enabling method was the electronic computer-aided design software, with which the engineers used the existing computers to calculate and simulate increasingly more complex electronic circuits, to inspire and automatically design next-generation higher-performance processors.

Similarly, simulations of quantum processors will play a central role in designing large-scale quantum computers (1-5). This requires us to calculate the basic properties of the target quantum electrocircuits, such as their energy spectra, coupling strength, and noise sensitivity (6). While these calculations could be done classically on a small scale, it is expected that the resources required for the classical simulations grow exponentially with the scale of the quantum hardware. Therefore, an important direction is to exploit the simulation capability of intermediate-scale quantum computers—for instance, those before full-fledged for prime factoring—to effectively aid the design of future higher-performance quantum computers (Fig. 1).

Variational quantum eigensolver (VQE) has emerged as a powerful quantum algorithm for simulation of the behavior of quantum system (7-10). In this work, we demonstrate quantum-aided design of a new high-performance qubit based on variational quantum simulation of a superconducting electronic circuit model. The discovered new qubit has a remarkable feature superior to the widely used transmons as it eliminates the charge noise but without sacrificing anharmonicity and thus shows a larger anharmonicity than transmons (5,11). The new qubit is fully compatible with the control technologies as in the transmon, exhibits a long coherence time, and can bring key advantages, including a shrinking physical size, improving the gate fidelity (12) and readout fidelity (5), reducing state leakage (13), and alleviating frequency crowding problem (14) in multi-qubit devices.

We start from the variational quantum simulation of the energy spectrum for a superconducting electronic circuit model (Fig. 1B), which provides the crucial property to identify the new qubit. The circuit has a shunted Josephson junction array as

inductance, which adds more complexity to the device but at the same time provide more design flexibility. The single Josephson junction in this system is parametrized by its Josephson energy E_J , while the capacitance and inductance can be parametrized by the capacitance and inductance C and L , or equivalently by $E_C = e^2 / 2C$ and $E_L = (\hbar / 2e)^2 / L$, which is the charging and inductive energy, respectively. The Hamiltonian of this circuit can be written as (15)

$$H = -4E_C \hat{n}^2 - E_J \cos(\hat{\phi} + \phi_{ext}) + \frac{1}{2} E_L \hat{\phi}^2 \quad (1)$$

where ϕ is the phase across the inductance, and n is the number of cooper pairs tunneled between the two islands of the circuit which is conjugate to ϕ . ϕ_{ext} is the external flux threading through the loop between the Josephson junction and inductance, in unit of the reduced superconducting flux quantum $\Phi_0 / 2\pi = \hbar / 2e$. As the quantum variables n and ϕ are both continuous, we will use the Fock-state basis of its harmonic part $H_{har} = -4E_C \hat{n}^2 + \frac{1}{2} E_L \hat{\phi}^2$ to discretely encode the system Hamiltonian.

Let a and a^\dagger be the annihilation and creation operator, the whole circuit Hamiltonian becomes

$$H = \omega \hat{a}^\dagger \hat{a} - E_J \cdot \frac{\hat{D}(iA)e^{i\phi_{ext}} + \hat{D}(-iA)e^{-i\phi_{ext}}}{2} \quad (2)$$

where $\omega = \sqrt{8E_C E_L}$ is the transition frequency of H_{har} , $A = (2E_C / E_L)^{1/4}$, and \hat{D} is the displacement operator defined as $\hat{D}(\alpha) = \exp(\alpha \hat{a}^\dagger - \alpha^* \hat{a})$. We truncate the Hilbert space to finite dimensions so that it can be mapped to the computational basis of our quantum processor. Here, we keep the Fock states up to 7 photons (Fig. 2A), which has enough accuracy for our quantum simulation.

The variational quantum circuit is shown in Fig. 2B. The role of this circuit is to implement unitary rotation from the computational bases (Fock states) to the energy eigenstates. The circuit consists of two 2-qubit and two 3-qubit \sqrt{iSWAP} gates (see

SI) with embedding variational single-qubit gates on both sides of them. In this work, we utilized the subspace-search VQE algorithm to find the lowest three energy eigenstates simultaneously (16). We initialize the quantum state in the lowest three Fock states and then execute the same unitary quantum circuit. As the input states are orthogonal, the final states after the circuit are also orthogonal. Therefore, by measuring the expectation value of Hamiltonian (Fig. 2C), we obtain the expected energies of the three orthogonal states, which are labelled E_0 , E_1 and E_2 . We define the cost function for variational optimization of the quantum circuit as

$$F_{\text{cost}} = 5 \times E_0 + 4 \times E_1 + 2 \times E_2,$$

where the weighing coefficients for lower eigenstates are larger than higher eigenstates. Thus, when the cost function is optimized to its global minima, the three output orthogonal states will be the three lowest eigenstates automatically.

In our algorithmic experiment, the design parameter E_L , the inductive energy of the Josephson junction array, is swept from 0.2 GHz to 3 GHz while the other parameters are fixed at $E_C = 0.7$ GHz, $E_J = 4.5$ GHz and $\phi_{\text{ext}} = \pi / 2$. Figure 2D shows the cost function and the corresponding energies of the three orthogonal states (the inset figure) as a function of the number of iterations in a typical example of the optimization process at $E_L = 3.0$ GHz. The cost function is optimized by the simultaneous perturbation stochastic approximation method (17). We observe a competition phenomenon in the energies during the optimization: the energies of 1st and 2nd excited states first decrease and then increase to the steady values, while the cost function decreases gradually. After completely sweeping the design parameter E_L , we plot the energy spectrum of the three lowest eigenstates as a function of E_L in the Fig. 2E. We see that the results agree well with the ideal values and interestingly, the excited states have smaller average deviated energies (~ 0.52 GHz) than the ground state (~ 0.76 GHz). The reason is that, in contrast to the excited states, the quantum state error in the ground state can only increase the energy. These energy deviations are partly contributed from the white noise

through the circuit decoherence, which can be reduced by quantum error mitigation method (see SI). The results before and after error mitigation are represented by circles and crosses in Fig. 2E, respectively. We see that the average deviations of energy estimation have reduced by 67%.

In the energy spectrum, we observe an anti-crossing signal between the two excited states when the inductive energy E_L is ~ 0.45 GHz, which indicates the presence of a phase transition. The phase transition is originated from the multiple valley profile of the potential in the system Hamiltonian. The physical picture is shown in Fig. 3A and 3B. Before the transition, the potential has two lowest valleys located around phase 0 and 2π (Fig. 3A for $E_L = 0.2$ GHz) and the eigenstates $|0\rangle$ and $|1\rangle$ localized in different valleys. As the parameter E_L increases, all of the potential valleys together with the eigenstates localized in them are lifted up. When the energies of excited eigenstates $|1\rangle$ and $|2\rangle$ in different valleys become closer, there exists an anti-crossing in energy spectrum. When the parameter E_L further increases, there will be only one potential valley left in phase space, and the lowest two energy states are both located in this single valley (Fig. 3B for $E_L = 2.0$ GHz). In fact, the parameter regime corresponding to the left side of the anti-crossing is the so-called heavy Fluxonium (18). Because of the small overlap of the wavefunctions for computational bases in different valleys, this type of qubit possesses large relaxation time up to 8 ms. However, the regime corresponding to the right side of the anti-crossing is never studied in previous works. In the followings, we will detailly discuss the qubit operated in this regime.

The potential profile of our new qubit resembles the transmon qubit but extends from $[-\pi, \pi)$ to the whole phase space. We call this new qubit Plasonium, because the qubit is driven by plasmon transition in single phase valley, which is in contrast to Fluxonium qubits using fluxon transition between two different phase valleys.

In Plasonium qubit, with the help of a shunted inductance, the charge degree of freedom

becomes a continuous variable and the charge bias noise can be fully eliminated through a gauge transformation. In this way, the tradeoff between anharmonicity and charge noise sensitivity in Transmon qubit are completely avoided. Thus, we are able to use a small shunt capacitance to increase the anharmonicity and reduce the device footprint without the influence of charge noise.

Except the elimination of charge noise, our Plasonium qubits keep high coherence time T_2 in a large tunable band of transition frequency. We compare the flux sensitivity of Plasonium with transmon and two other variants of the inductively shunted Josephson junction model, heavy Fluxonium and Quarton (19). Their energy dispersion $\partial f_{01} / \partial \phi_{ext}$ with external flux versus the transition frequency detuning from their first-order flux insensitive point is plotted in Fig. 3C (see SI). We observe that the flux sensitivity of Plasonium is much less than heavy Fluxonium and Quarton when detuned the same level from its flux-insensitive point. It is also less than the Transmon qubit with symmetric junctions. This is because the Plasonium can be viewed as a Transmon with a non-symmetric composite junction, including a single junction and a junction array, to reduce the flux sensitivity. Therefore, when neglecting the other decoherence channel which is usually small compared with flux noise, the Plasonium qubit has the largest high- T_2 frequency band (20).

Next, we move to the experimental test of the new qubits. In Fig. 4A, we show the scanning electron microscopy (SEM) image of the fabricated Plasonium qubits, which has qubit length of $240 \mu\text{m}$, only 40% of a typical transmon. The key element, the inductance of $E_L = 2.20 \text{ GHz}$, is implemented by 37 large-area Al/Al oxide/Al Josephson junctions connected in series (21,22). In our samples, we keep the structure of Plasonium to like Transmon to the most extent, where the qubit's frequency is tuned by an inductively coupled transmission line (TL), the qubit's transition is driven by another capacitively coupled TL, and the qubit is measured by probing a dispersively coupled resonator through a readout TL (Fig. 4A). Therefore, our qubits have a good

compatibility with Transmon's operating system, which is widely used in contemporary quantum computing experiments.

We first experimentally measure the energy spectrum of the qubit transitions. We apply an X gate to initialize the qubit in $|1\rangle$ state, and then tune the external flux threading the Josephson loop to different bias points where we apply microwave pulses with varying frequencies to probe the transition frequencies f_{01} and f_{12} . The resulting energy spectrum of our Plasonium qubit is shown in Fig. 4B, from which we extract parameters to be $E_C = 0.60$ GHz, $E_J = 5.61$ GHz and $E_L = 2.20$ GHz, agreeing well with our design. In Fig. 4B, the green and red solid line is the theoretic fit of the spectrum indicating f_{01} and f_{12} 's dispersion with the external flux. The additional gray dotted line is due to the non-ideal input of microwave driving signal. From the data, we see the anharmonicity has a minimum 490 MHz at the flux insensitive point, which is about 50% larger than the typical Transmons and can reduce the state leakage error by 55%. We note that this anharmonicity is not the upper bound of Plasonium because it can be further increased by reducing the capacitance of the qubit.

We continue to measure the coherence properties of the Plasonium qubit. At its flux insensitive point, we measured its relaxation time $T_1 = 32.5 \pm 1.2$ μ s and dephasing time $T_2 = 16.3 \pm 0.9$ μ s through Ramsey interferometry (Fig. 4D). This result is slightly better than the best transmon qubit fabricated on the same chip. In Fig. 4C, we present the measured coherence time at different flux detuning. The result shows that the new qubit still keeps the dephasing time above 2 μ s when detuning from flux insensitive point as much as 400 MHz, which demonstrates a large high- T_2 frequency band. We further characterize the quantum gate performance of the new qubit by randomized benchmarking (23,24). Fig. 4E shows the average fidelity of a single X/2 gate is 99.84(7)%. We note that this is the first batch of the new qubit device we fabricated. With recent progress in new superconducting materials and surface

treatment method (25-27), we expect that the lifetime and coherence time of Plasonium qubits can be improved to several hundreds of microseconds.

The Plasonium qubit is operated in a new favorable parameter regime that is discovered with the help of an efficient quantum simulation of a quantum electrocircuit. The new qubit composes a Josephson junction array like Fluxonium qubits but operates through plasmon transition in single phase valley. The qubit has two lowest localized states in the same potential valley to encode an advanced qubit, which can be viewed as an improved transmon qubit with larger anharmonicity and smaller footprint. In addition to the potential advantages, the Plasonium qubit shares many features as transmon, therefore, in the future work, we can make use of established technology in the transmon qubit to optimize the Plasonium and use it to construct multi-qubit devices. For example, entangling gates can be realized by coupling qubits capacitively, a long-range interaction can be implemented with the help of a transmission line resonator (28), and the readout fidelity can be improved by the multilevel measurement protocol (29,30).

In summary, we have proposed and demonstrated quantum computer-aided design to discover and test a new high-performance superconducting qubit, the Plasonium. Our results indicate that using small-scale quantum simulators to automatically design and optimize more advanced quantum processors is a promising route in scaling up practical quantum computers.

References and notes

1. M. H. Devoret, R. J. Schoelkopf, *Science*. **339**, 1169–1174 (2013).
2. J. E. Mooij, *Science*. **285**, 1036–1039 (1999).
3. J. Q. You, X. Hu, S. Ashhab, F. Nori, *Phys. Rev. B*. **75**, 140515 (2007).
4. F. Yan *et al.*, *Nat Commun*. **7**, 12964 (2016).
5. J. Koch *et al.*, *Phys. Rev. A*. **76**, 042319 (2007).
6. P. Krantz *et al.*, *Applied Physics Reviews*. **6**, 021318 (2019).
7. C. Hempel *et al.*, *Phys. Rev. X*. **8**, 031022 (2018).

8. F. Arute *et al.*, *Science*. **369**, 1084–1089 (2020).
9. A. Kandala *et al.*, *Nature*. **549**, 242–246 (2017).
10. T. H. Kyaw *et al.*, *arXiv:2006.03070* (2020).
11. J. A. Schreier *et al.*, *Phys. Rev. B*. **77**, 180502 (2008).
12. A. D. Cárcoles *et al.*, *Phys. Rev. A*. **87**, 030301 (2013).
13. Z. Chen *et al.*, *Phys. Rev. Lett.* **116**, 020501 (2016).
14. J. B. Hertzberg *et al.*, *npj Quantum Inf.* **7**, 129 (2021).
15. V. E. Manucharyan, J. Koch, L. I. Glazman, M. H. Devoret, *Science*. **326**, 113–116 (2009).
16. K. M. Nakanishi, K. Mitarai, K. Fujii, *Phys. Rev. Research*. **1**, 033062 (2019).
17. J. C. Spall, *IEEE Trans. Automat. Contr.* **37**, 332–341 (1992).
18. N. Earnest *et al.*, *Phys. Rev. Lett.* **120**, 150504 (2018).
19. F. Yan *et al.*, *arXiv:2006.04130* (2020).
20. D. Sank *et al.*, *Phys. Rev. Lett.* **109**, 067001 (2012).
21. N. A. Masluk, I. M. Pop, A. Kamal, Z. K. Mineev, M. H. Devoret, *Phys. Rev. Lett.* **109**, 137002 (2012).
22. D. V. Nguyen, D. M. Basko, *Eur. Phys. J. Spec. Top.* **226**, 1499–1514 (2017).
23. E. Knill *et al.*, *Phys. Rev. A*. **77**, 012307 (2008).
24. E. Magesan *et al.*, *Phys. Rev. Lett.* **109**, 080505 (2012).
25. A. P. M. Place *et al.*, *Nat Commun.* **12**, 1779 (2021).
26. A. Osman *et al.*, *Appl. Phys. Lett.* **118**, 064002 (2021).
27. M. Mergenthaler *et al.*, *Review of Scientific Instruments*. **92**, 025121 (2021).
28. C. Song *et al.*, *Science*. **365**, 574–577 (2019).
29. S. S. Elder *et al.*, *Phys. Rev. X*. **10**, 011001 (2020).
30. C. Wang, M.-C. Chen, C.-Y. Lu, J.-W. Pan, *Fundamental Research*. **1**, 16–21 (2021).

Figure Captions

Fig. 1| The concept of quantum design. (A) Quantum design uses the existing

quantum computing resource to accelerate the development of next-generation quantum computers. It plays the same role of electronic computer-aided design for classical computers, which has great achievements in the past decades. **(B)** The outline of our work. We used a variational quantum eigensolver to simulate a superconducting quantum electronic circuit. The circuit model has a Josephson junction array as a shunted inductance. We fabricated and tested the new qubit guiding by the quantum simulation result and obtain an advanced qubit with better performance than the transmon. We named the new qubit as Plasonium.

Fig. 2| Variational quantum simulation. **(A)** Fock states up to 7 photons used as the bases to encode the system Hamiltonian. **(B)** The variational quantum circuit used to rotate the Fock states to the eigenstates. It has 26 variational parameters in the embedded single-qubit gates. The cost function is defined as a weighting sum of the three lowest energy eigenvalues: E_0 , E_1 and E_2 . **(C)** The system Hamiltonian shown in the Fock bases. It is mapped to a weighting sum of Pauli operators (20 terms) through Gray code to estimate the energy eigenvalues. **(D)** A typical optimization process for design parameter $E_L = 3.0$ GHz. The inset shows the three lowest energy eigenvalues as a function of the number of iterations. **(E)** The energy spectrum of the three lowest eigenvalues as a function of the parameter E_L . The error mitigated values are also shown.

Fig. 3| Characteristics of the new qubit. **(A)(B)** Potential profile of the system Hamiltonian and the corresponding energy eigenvalues before ($E_L = 0.2$ GHz) and after ($E_L = 2.0$ GHz) the phase transition, respectively. **(C)** Flux noise sensitivity as a function of the detuning from the flux insensitive point. Four types of qubits are put into comparison: Transmon, Heavy Fluxonium, Quarton and Plasonium.

Fig. 4| Fabrication and test of the new qubit. **(A)** The optical images of the Plasonium

qubit. The geometry layout of the new qubit is similar to the transmon qubit. The zoom-in shows the inductively shunted Josephson junction array. **(B)** The transition spectrum of the Plasonium qubit as a function of the external flux. The $|0\rangle \leftrightarrow |1\rangle$ and $|1\rangle \leftrightarrow |2\rangle$ transitions are observed. **(C)** The dephasing time as a function of the detuning from its flux insensitive point. **(D)** The energy relaxation time and the dephasing time measurement at the flux insensitive point. **(E)** The randomized benchmarking of single-qubit gates.

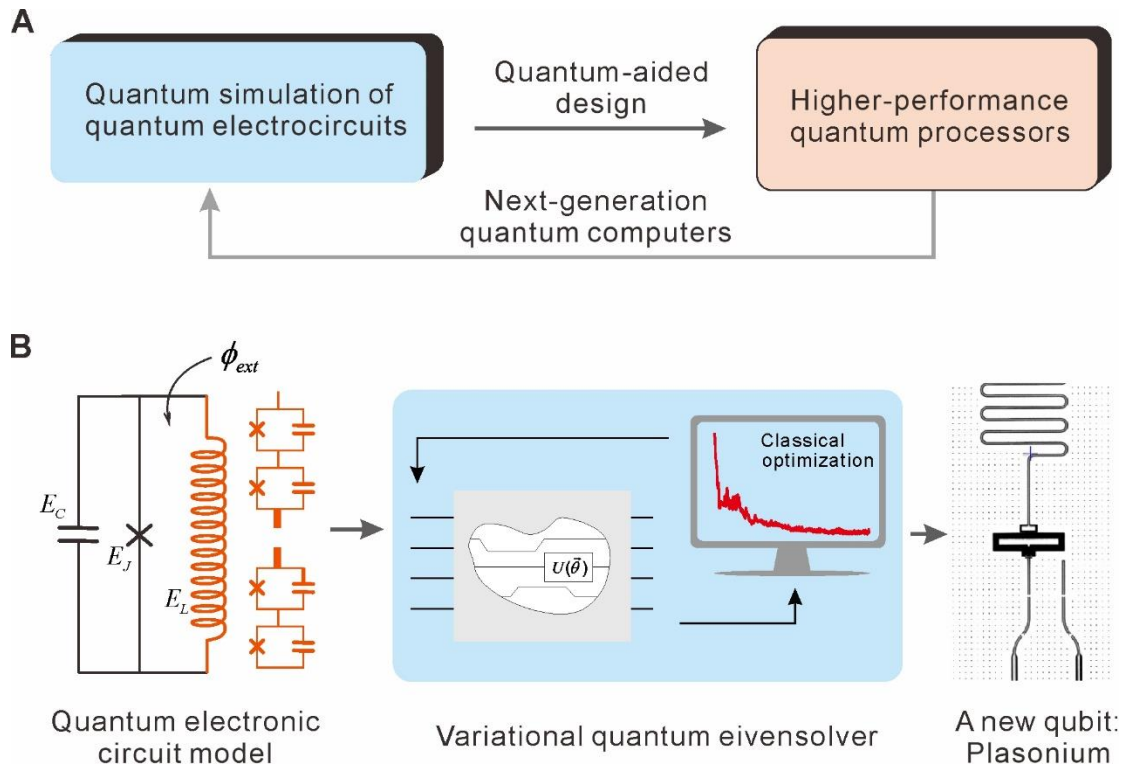


Figure 1

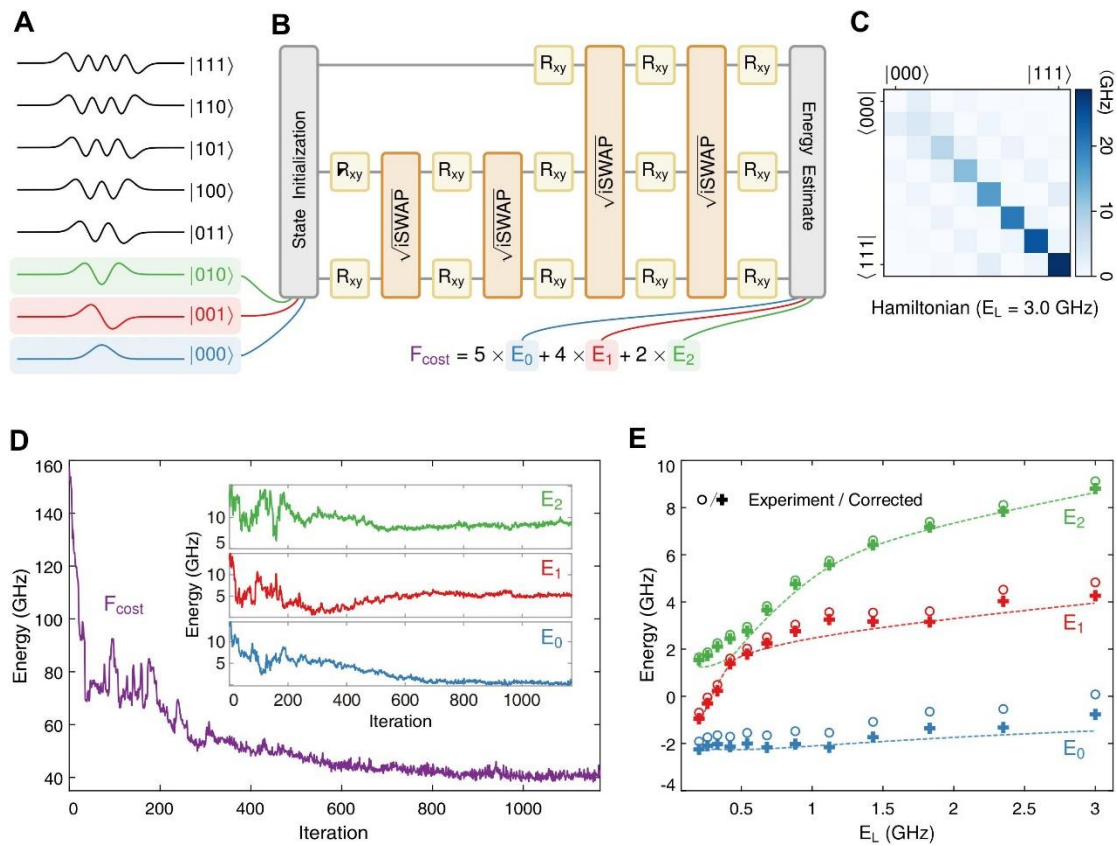


Figure 2

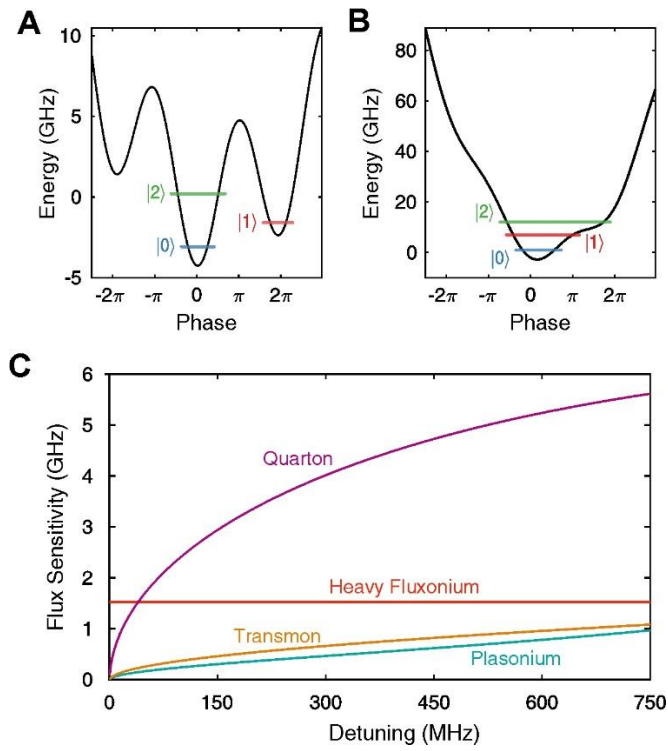


Figure 3

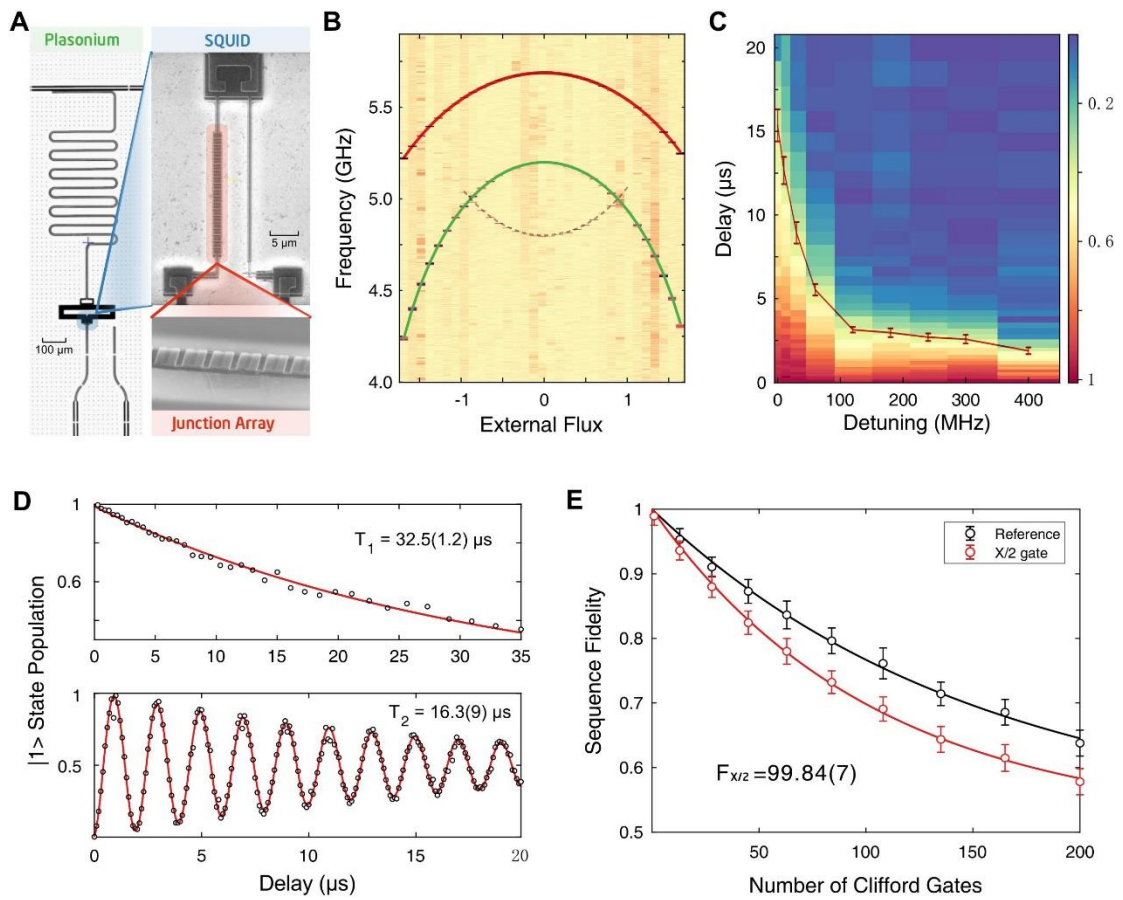


Figure 4